The morphology and evolution in Al-Cu and Al-Fe magnetic pulse weld interfaces characterized through phase-contrast micro-tomography

Benjamin Zielinski, Tarik Sadat, Bratislav Lukić, Alexander Rack, Eric Markiewicz, Laurent Dubar

Tomography of Materials and Structures 3 (2023) 100018

Contents lists available at ScienceDirect

Tomography of Materials and Structures

journal homepage: www.journals.elsevier.com/tomography-of-materials-and-structures

The morphology and evolution in Al-Cu and Al-Fe magnetic pulse weld interfaces characterized through phase-contrast micro-tomography

Benjamin Zielinski [a,b,*], Tarik Sadat [a], Bratislav Lukić [c], Alexander Rack [c], Eric Markiewicz [a], Laurent Dubar [a]

[a] Univ. Polytechnique Hauts-de-France, CNRS, UMR 8201 - LAMIH, F-59313 Valenciennes, France
[b] INSA Hauts-de-France, F-59313 Valenciennes, France
[c] ESRF – The European Synchrotron, CS40220, CEDEX 09, 38043 Grenoble, France

ARTICLE INFO

Keywords:
Magnetic pulse welding
Interface
Morphology
X-ray micro-computed tomography
Synchrotron microtomography

ABSTRACT

Magnetic Pulse Welding (MPW) facilitates the permanent joining of dissimilar metallic materials through the sudden impact generated by a magnetic pulsed field. The process can introduce distinct morphological features at the interface of bi-material joints, which subsequently affect the joint's quality and durability. This article delves into the investigation and quantification of various interfacial morphologies in Aluminum/Copper and Aluminum/Steel joints, using high-energy phase-contrast synchrotron micro-tomography. Surface topography is extracted from 3D tomographic datasets between dissimilar materials, enabling a comprehensive comparison between different material pairings and various locations within the weld. The study analyses and compares the roughness parameters of these surfaces. Moreover, it describes the interface's waves and vortexes through diverse morphological metrics, encompassing their shape and size. The results provide evidences that vortexes evolve in three dimensions, with lateral growth and collapse. The waves and vortexes shapes promote material interlocking, increasing the contact area between the dissimilar materials by up to 20%. The interface morphology of Al/Cu joints exhibits higher roughness and a greater number of vortexes compared to Al/Fe joints. Lastly, the findings reveal the presence of interface damage in the form of pre-existing discontinuities.

1. Introduction

Industrial engineering focuses on continually improving metallic materials and structures, enhancing their properties, and extending their application to extreme scenarios. This heightened use, reaching the material's limit state, leads to increased quality requirements ensuring defect-free manufacturing to maintain component functionality. Quantitative nondestructive evaluation (QNDE) enables the assessment of material or structural deterioration, by bulk detection and characterization of discrete flaws in structures or parts before they reach a point of rupture or are deployed in industrial conditions [1].

QNDE encompasses various techniques based on different physics and applications, such as Pulsed Eddy-Current (PEC) which uses induced electro-magnetic fields and current to perform structural integrity inspection and material characterization [2]. However, the inspection can be limited by the depth of penetration which is directly connected to the skin depth. An example is ultrasonic testing which enables to detect internal defects in sound conducting materials [3] by using elastic waves in the material.

X-ray micro computed-tomography[1] (μ-CT) is a nondestructive technique that enables the examination of a material's internal volume and microstructure [4], offering valuable 3D volumetric information like phase fractions, phase contiguity, porosity [5], or damage levels [6]. This information is essential for assessing solid-state welding techniques that can lead to cracks or voids in highly deformed materials [7].

In the specific case of Aluminum/Steel joints produced by friction stir welding, X-ray μ-CT was employed to quantify porosities and porosities and their distribution [8], thereby aiding in understanding pore interconnectivity within the volume. Recently, X-ray μ-CT has found new applications due to improved methods and equipment [6]. It can be used to extract the shape and surface characteristics of multi-materials components [9], evaluating their dimensions and conducting

* Corresponding author at: Univ. Polytechnique Hauts-de-France, CNRS, UMR 8201 - LAMIH, F-59313 Valenciennes, France.
E-mail address: benjamin.zielinski@outlook.com (B. Zielinski).

[1] X-ray micro computed-tomography refers to tomographic techniques in general with micrometers voxel size resolution. X-ray sources can either be a laboratory or a synchrotron.

https://doi.org/10.1016/j.tmater.2023.100018
Received 6 September 2023; Received in revised form 16 October 2023; Accepted 31 October 2023
Available online 8 November 2023

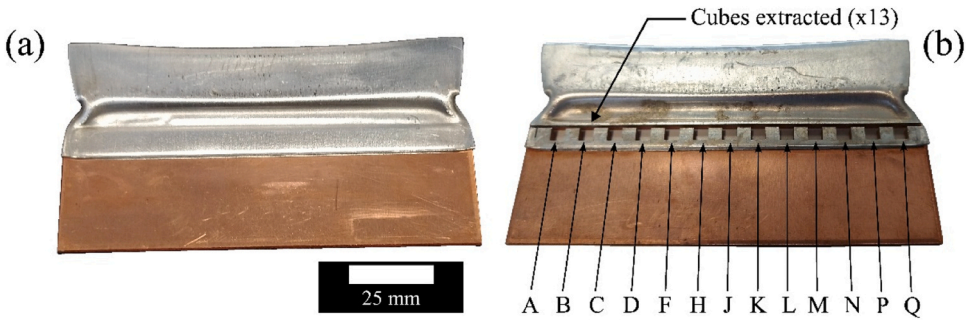

Fig. 1. Al/Cu joint produced by MPW, (a) – Before cutting, (b) – Naming convention after cubes extraction in the middle of the joint.

Table 1
MPW specimens analyzed.

Sample number	Materials couple	Section							
		A	B	C	D	F	H	J	K
1	Al/Fe							X	
1	Al/Cu	X	X	X	X	X	X		
2	Al/Cu						X	X	X
3	Al/Cu						X	X	

topographic analysis, including roughness parameter calculations [10]. Such surfaces may contain re-entrant features, such as undercuts in additive manufacturing [11], which are challenging to measure using conventional methods [12]. Nevertheless, accessing detailed microstructural information within high Z-materials at the sub-micrometer level remains a challenge for current laboratory X-ray sources, with limitations in scanning time, sample preparation and resolving power. Combining X-ray μ-CT with a synchrotron source can bridge this gap, offering finer microstructural details thanks to high-brilliance in hard X-ray regimes and state-of-the-art equipment [13]. The benefits result in smaller achievable voxel size, improved contrast at material interfaces due phase contrast modality given the partial coherence and small source size, access to chemical analyses, among others [14]. Therefore, synchrotron-based X-ray μ-CT is a crucial method for microscale examination of Magnetic Pulse Welding (MPW) joints.

MPW, a part of high-velocity impact welding (HVIW), is a solid-state welding technique with roots in the 1960–1970 s when it was initially

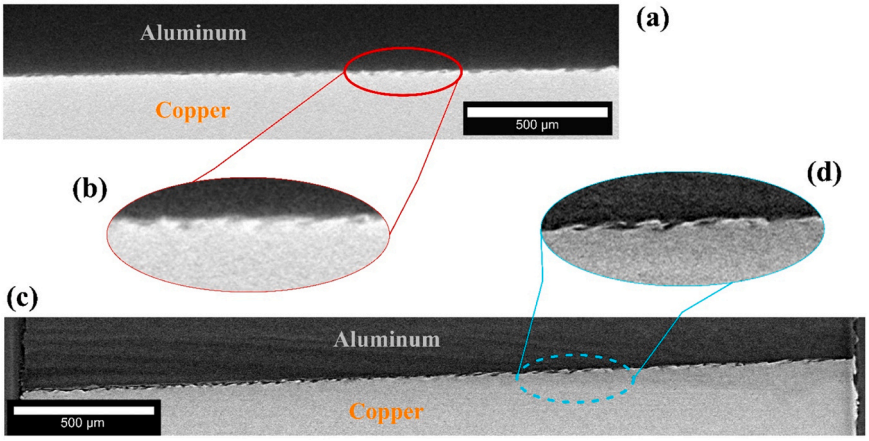

Fig. 2. Comparison of a tomographic section for an Al/Cu interface MPW joint, (a) – Laboratory X-ray absorption tomographic section, (b) – Close-up of the interface for the laboratory source, (c) – Synchrotron propagation-based phase contrast section, (d) – Close-up of the interface for the synchrotron source.

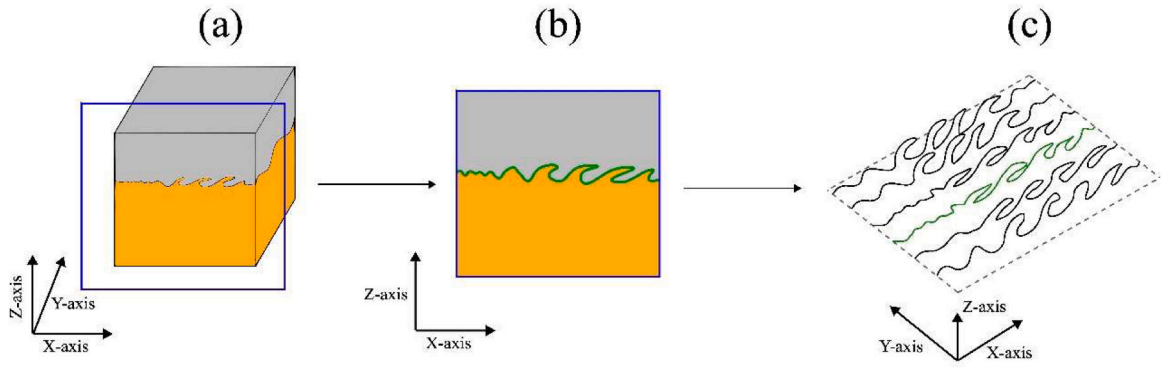

Fig. 3. Main steps of the program to extract and analyze the interface surface, (a) – Selection of a section from the tomographic data, (b) – Pre-process of the data (filtering), interface line extraction, vortex parameters computation (c) – Collection of interface lines and surface exportation.

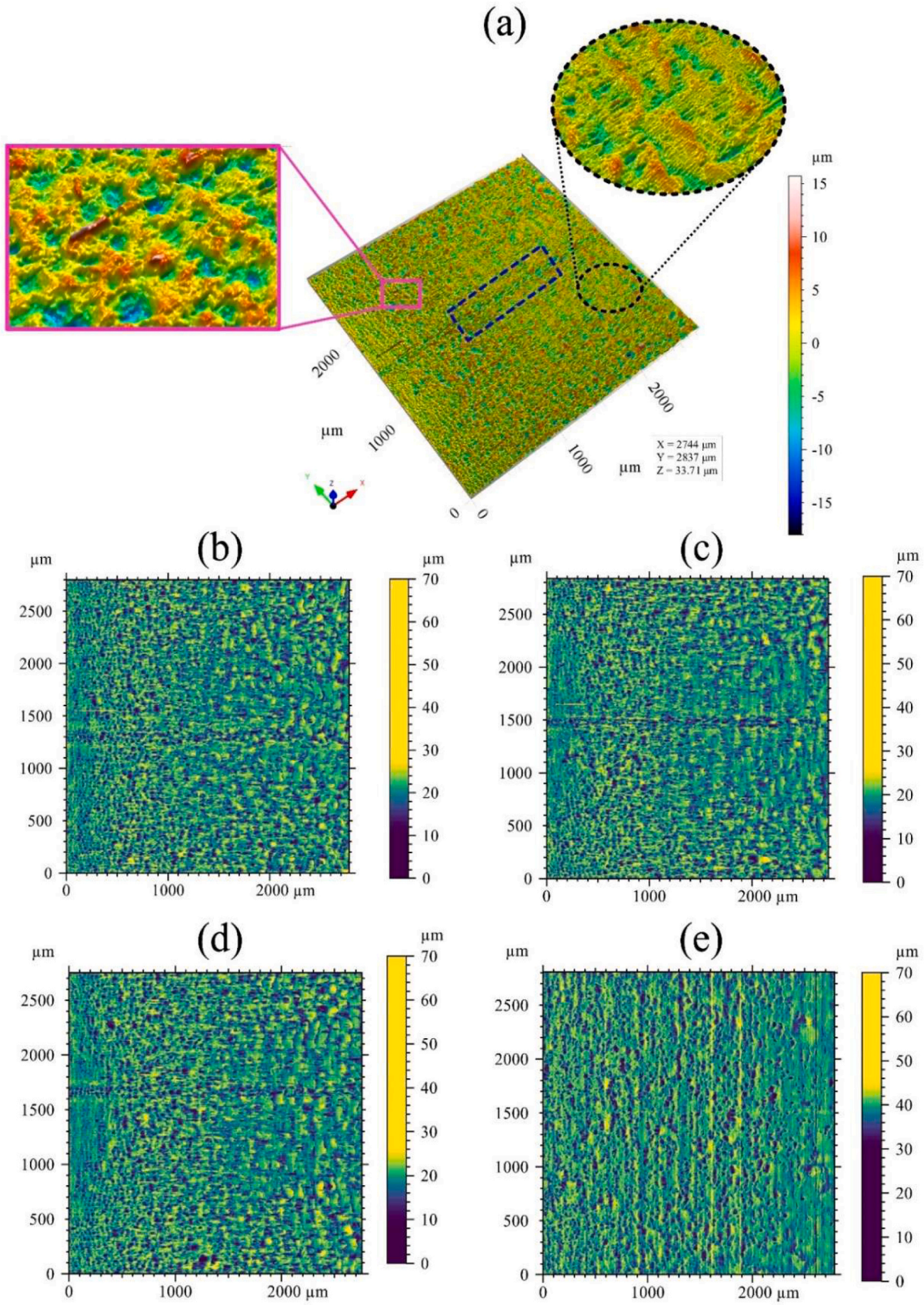

Fig. 4. Height average surface maps from Al/Cu and Al/Fe interfaces (a) 3D view from Section J2 – Al/Cu, -(b) Surface top view section H2, -(c) Surface top view section J2 – Al/Cu, -(d) Surface top view section K2 – Al/Cu, -(d) Section K, -(e) Surface top view section J – Al/Fe specimen.

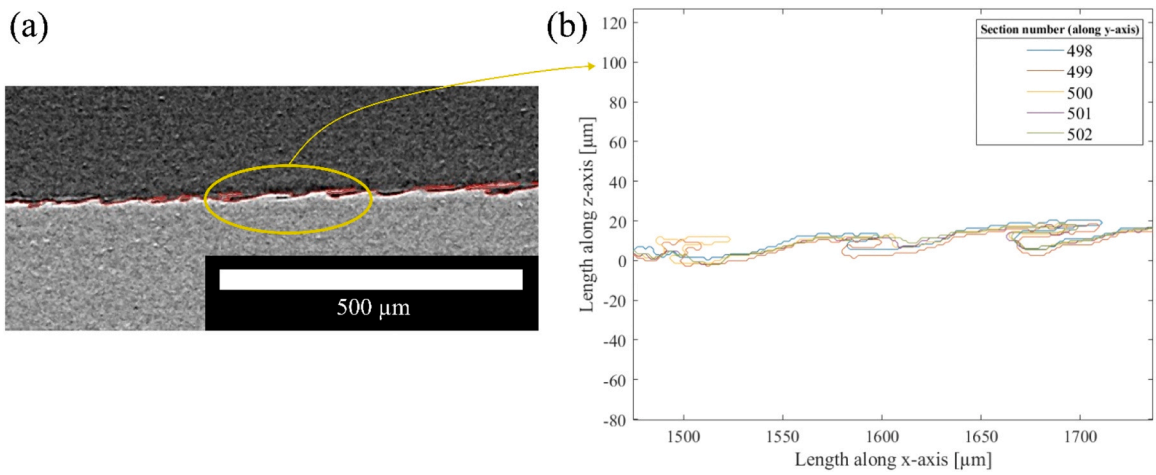

Fig. 5. Interface line extraction – (a) Overlay of the extracted interface line (red) on the tomographic data from section 500, -(b) Plot of the surroundings interface lines around section 500.

used for joining nuclear fuel rods [15]. It is now widely employed in various industrial applications, including automotive driveshaft production [16], nuclear sectors [17], and more recently, the aeronautics industry due to its ability to weld alloys like the 7000 series aluminum, which are difficult to weld conventionally [18]. In MPW, collision speed range from 300 to 700 m.s^{-1}, and the joining process is completed in under 100 µs [19]. The collision is produced between a mobile element (called flyer) and a fixed element (called receiver or target). It is an energy efficient and also environmentally friendly process that relies on an electromagnetic discharge [20]. It does not produce fumes or consume shielding gases as TIG welding. MPW enables the welding of dissimilar material pairs that cannot be conventionally welded without the formation of a thick intermetallic compound (IMC) layer [21], such as Aluminum/Copper (Al/Cu) or Aluminum/Steel (Al/Fe). Al/Cu dissimilar welds are employed in thermal or electrical applications, while Al/Fe joints are utilized to reduce the weight of structural components [20]. However, due to the high strain rates during collision and the variable impact velocity and angle, instabilities are created at the interface by the velocity shearing between the two materials [22]. This is leading to the formation of distinctive features like waves, vortexes, and cavities [23]. Waves and vortexes are considered to strengthen the produced joint [24]. These features serve as evidence of the conditions encountered during the process. Typically, MPW features are examined through 2D cross-sections using optical or electron microscopy images [25] measuring their size and amplitude. Unfortunately, these techniques do not provide 3D information about these features and they are limited by their numbers.

In this paper, Al/Cu and Al/Fe joints produced by MPW are analyzed using synchrotron high-energy phase contrast tomography to describe and quantify the various features at the interface between the two dissimilar materials. X-ray µ-CT can offer 3D information about the waves and vortexes at the interface, which could explain the mechanisms behind the formation of these features. We can emphasize the qualitative work done by Lee et al. [26] about waves morphology on Cu/Ti joints produced by MPW through X-ray analysis as probably the only study done on this topic. We expect also to confirm that meso-scales cavities inside the vortexes are not interconnected [27].

2. Materials and methods

2.1. Samples preparation

The samples used in this study are dissimilar joint welds of Al/Cu and Al/Fe, which were produced using the MPW technique. These joints were fabricated using a Pulsar 25 kJ - 9 kV device equipped with a 690 µF condenser, operating at a theoretical frequency of 25 kHz utilizing a flat coil at PFT Innovaltech (France). This same device has been previously employed in other studies [28,29]. The materials used consisted of 1 mm thick commercial sheets of 1050 Aluminum and S300 steel, as well as a 2 mm thick commercial sheet of pure Copper. In both combinations (Al/Fe and Al/Cu), aluminum served as the flyer part, while copper or steel acted as the target material. Flat joints were created with an overlapping configuration, resulting in a final dimension of approximately 98 × 53 mm^2.

Fig. 1(a) illustrates the aspect of the weld after the processing stage. The process parameters were identical for both cases in terms of collision velocity and impact angle. Process parameters included an electrical energy level of 19.4 kJ, a 2 mm gap, and a 7 mm overlap.

To examine the local details of the weld microstructure, cubic specimens measuring 3 × 3 × 3 mm^3 for Al/Cu and 3 × 3 × 2 mm^3 for Al/Fe samples were extracted from the primary joint using Wire-Cut Electrical Discharge Machining (WEDM). Schematics showing the locations of the extracted specimens are displayed in Fig. 1(b). Each sample was carefully engraved to ensure proper traceability of origin following a designated naming convention.

During this study 12 samples were characterized, each originating from different joints, locations, and material combinations. The experimental conditions are outlined in Fig. 1 and Table 1. The selection of various specimens aimed to assess the variation of the weld interface within a specific sample (Al/Cu sample n°1 – sections A to H) and to compare the stability of a section (H) across three samples (H1, H2 and H3) from Al/Cu joints. Additionally, a comparison was conducted between Al/Cu and Al/Fe samples for the J-section. Based on the external deformation of the flyer, we anticipated that sections C to N would display a similar interface morphology, whereas sections A-B and P-Q would have different characteristics due to edge effects during the welding process.

2.2. Synchrotron-based high-energy phase contrast micro-tomography

The micro-tomography acquisition was conducted at the ID19 beamline of the European Synchrotron Radiation Facility (ESRF, France) [30]. The imaging conditions involved illuminating the sample with a filtered white beam during its continuous rotation over 360 degrees. The selected radiation source was a wiggler insertion device, and its emitted radiation was filtered with a series of attenuators along the vacuum flight tube to produce a spectrum with a peak photon energy at 80 keV. The experiment was located 145 m from the source, and the indirect detector assembly was positioned 0.2 m downstream of the sample. Within this configuration, the propagation-based phase contrast took

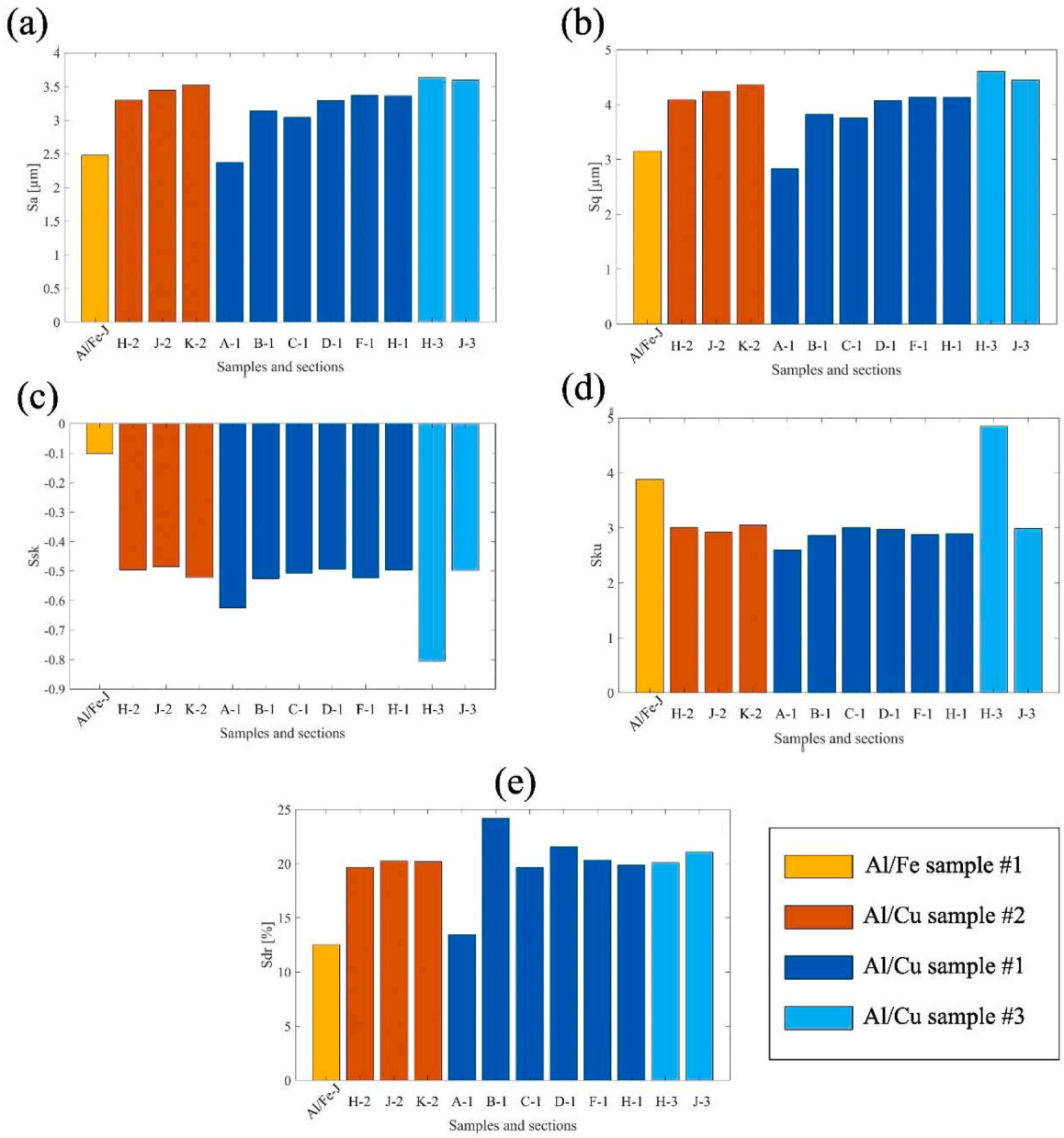

Fig. 6. Topographic roughness parameters analysis on the surfaces extracted from the interfaces – (a) Sa parameter, - (b) Sq parameter, -(c) Ssk parameter, -(d) Sku parameter, -(e) Sdr parameter.

effect thanks to the partial spatial coherence of the incoming wavefronts reaching the experimental hutch. The indirect detector consisted of 250 µm thick LuAG:Ce (Ce- doped $Lu_3Al_5O_{12}$) scintillator optically coupled with a microscope objective (Mitutoyo, M Plan Apo 5 ×, NA=0.14) *via* a mirror to a pco.edge 5.5 sCMOS camera (PCO AG, Germany). This detector arrangement is suitable for high dose applications since none of the optical components are directly exposed to the intense ionizing radiation.The resulting pixel size of the detector was 1.28 µm, with each recorded radiograph consisting of 2160 × 2560 pixels. Given the field of view, the entire sample was captured within a single tomographic scan for the width (horizontal view). However, there was a slight cropping for the vertical view (around 0.2 mm). The reconstruction was performed using the NABU reconstruction package and an in-line phase retrieval algorithm with ratio of the real and complex refraction index of 20 [31,32]. Post-processing was carried out with in-house scripts and included ring removal based on a spectral filtering method [33] and double flat field normalization to eliminate beam hardening. While the high-energy component of the radiation facilitated the penetration of high-Z materials within a short acquisition time (*i.e.*, one full tomogram of 6000 projections within 8 min), the propagation-based phase contrast modality significantly enhanced the detectability of interfacial features by increasing the contrast at the interface between different materials and phases. This feature was crucial in collecting underlying information at the interfaces between aluminum and copper and aluminum and iron at microscale, revealing microstructural content that is typically not accessible using conventional laboratory source, such as for example intermetallic compounds and micro cracks, for example.

Fig. 2 displays a comparison between a laboratory tomographic section and synchrotron high-energy propagation phase-contrast tomography along a vertical section within the bulk of the material. The laboratory source, which utilized a tungsten source and target, performed tomography using the commercial Ultra Tom tomography system (RX Solutions, France) from the ISIS4D regional platform located at

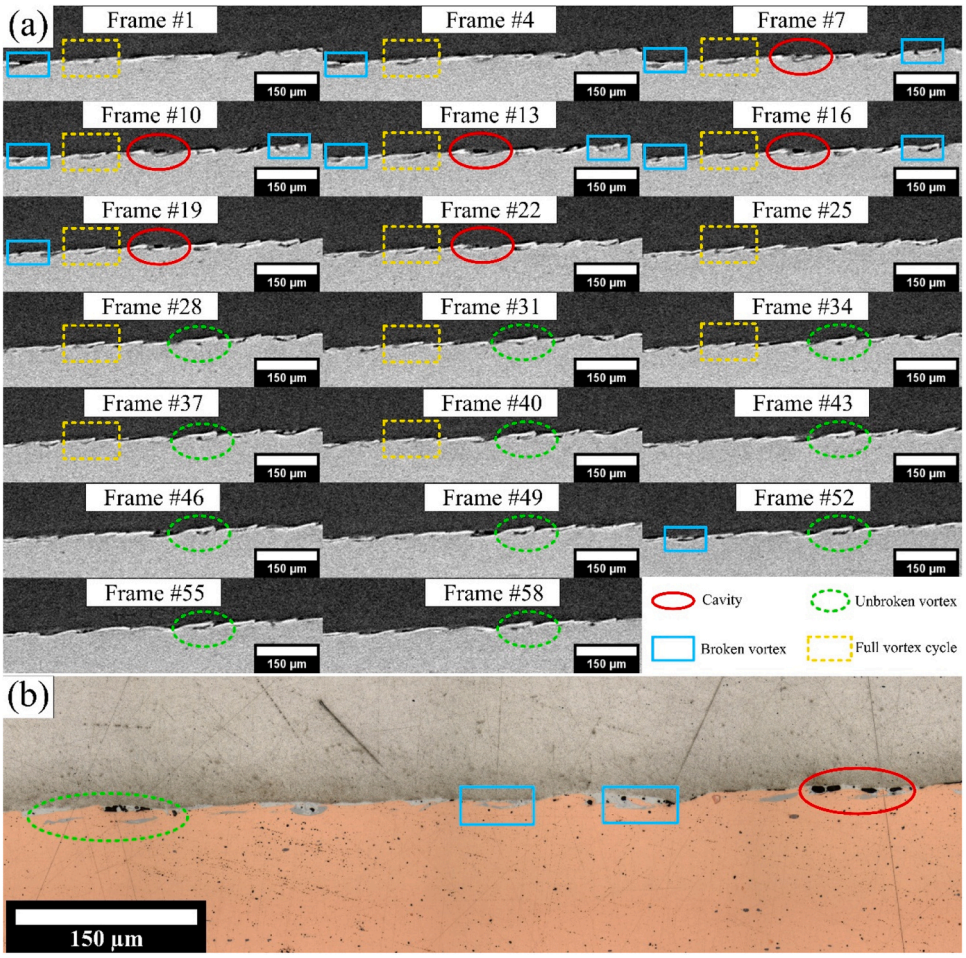

Fig. 7. Examples of MPW interfaces features (waves, vortexes and cavities) [aluminum is on top and copper on bottom for all the pictures], (a) - Synchrotron high-phase contrast microtomography frames, (b) - Optical image microscopy of an Al/Cu cross-section.

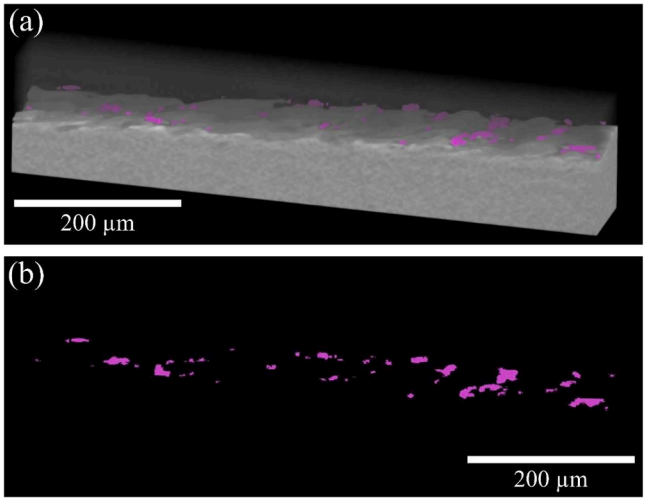

Fig. 8. Porosities and cavities localization from the Al/Cu cross-section presented in Fig. 7 – voxel size 1.28 µm, (a) – View with copper, aluminum and porosities (pink), (b) – View with porosities only.

the University of Lille (France). The experimental parameters included a voltage of 160 kV, a current of 89 µA, a spot size of 0.8 µm, and 1440 projections, were used during the experiments, resulting in a voxel size resolution of 1.74 µm. In Figs. 2(b) and 2(d), close-up views allow for a comparison of the imaged interface between the dissimilar materials. The reconstructed interface from the laboratory source, based on X-ray absorption, appeared less sharp than the interface imaged by the synchrotron source. The use of propagation-based phase contrast enhanced the contrast between copper and aluminum and revealed finer details on the features. This comparison demonstrates that the synchrotron-based radiation enables the acquisition of higher-resolution and well-contrasted information at the interface, including details about waves, vortexes, and intermetallic compounds, with reduced beam-hardening and absorption artifacts.

2.3. *Image analysis and feature extraction*

With access to the internal 3D structure of the samples through high-resolution tomographic data, several microstructural image analysis steps were employed to examine and analyze the interface between the dissimilar materials within the cubic samples, with a specific focus on features of MPW joints at the interface. The commercially available software DragonFly (Object Research System - ORS) was used for visualizating of the interface, including waves and vortexes [34]. However, for detailed profilometry extraction and analysis, a set of in-house codes using MATLAB [35] were developed allowing extracting and measure interface features and export the surfaces. This method is based on a discretization of the studied volume into 2D sections, and each section is analyzed using methods and definitions consistent with those employed in optical microscopy.

First, the data underwent pre-processing, which included applying a median filter (with a kernel size of 3 × 3 pixels) to remove outliers,

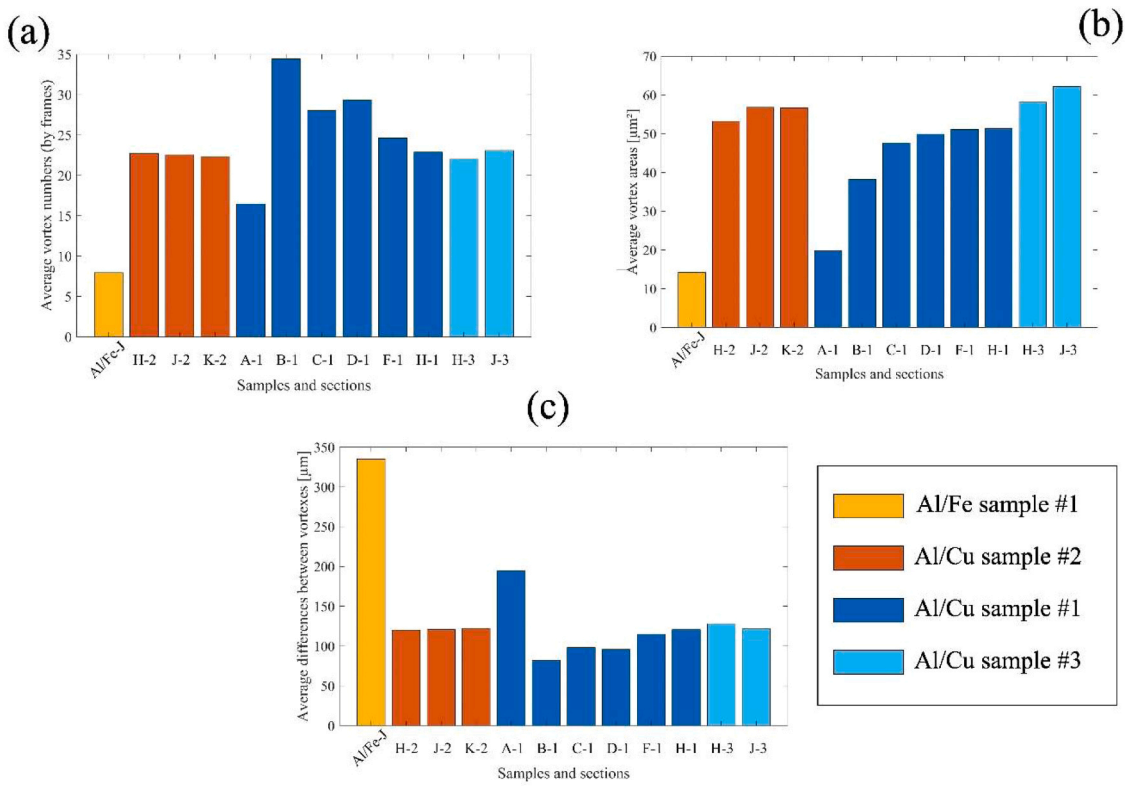

Fig. 9. Vortex parameters comparison, (a) – Average number of vortexes by frame, (b) – Average vortexes areas, (c) – Average distance between vortexes.

followed by an unsharp masking method using a Gaussian lowpass filter. Subsequently, the images were segmented based on automated Otsu segmentation, cleaned (to remove spurs and H-connections) and reduced to their contours. H-connections refer to a single pixel serving as a junction between two groups of pixels through this unique link (the letter H symbolizes this representation). This contour is taken as the corresponding interface line between the dissimilar materials.

From each 3D dataset, the interface border line was extracted between the two dissimilar materials on every tomographic section, on a slice-by-slice basis. The interface line extended continuously along the interface, including the backward direction for the interface features. This backward direction, also known as re-entrant cut, was used to determine whether it represented a wave or a vortex. A local gradient on the pixels coordinates was computed. In the case of a positive value, the feature was classified as a wave, and as a vortex for a negative value.

For each extracted line, the program calculated and saved information about the number, position, and size of the vortexes. These lines were then collected and exported as surfaces. The surfaces were converted into height maps, and roughness parameters were then computed using Mountains software (Digital Surf) [36]. The height maps were centered by the mean plane passing through all the data points.

A sketch outlining the main steps of the segmentation, computation and data exportation is depicted in Fig. 3. A detailed description of the methodology used can be found in a previous study by the authors [37].

To examine micro-cracks and porosities across the tested samples and between the two dissimilar materials, the tomographic data were visualized using Dragonfly software.

3. Results and discussion

3.1. Tomography-based surface topography

As previously explained in the Materials and Methods section, surfaces from the interface between the two dissimilar materials were extracted and visualized using the methods described in 3.2. This allows for the evaluation of data quality and provides an initial understanding of the interface's morphology.

Fig. 4 displays three different sections (H, J, and K) of the interface from Al/Cu and one section (J) from Al/Fe. Color bars for the height (z-axis) was set up on the maximum range applied to the different maps. Color bar is optimized to improve contrast for the different features. These maps represent an average value (z-axis) in cases where there are multiple values for the same X/Y coordinates pair. Similar features (height variations) are visible across all Al/Cu sections with a gradual evolution of shapes along the x-axis. This evolution of the interface morphology is due to the variations in the impact angle and velocity along the welding direction during the process. These variations have been extensively studied numerically in 2D, as demonstrated in the works of Xu [38] and Li [39]. Furthermore, these shapes and morphologies on the different surfaces exhibit similar sizes along the z-axis. It is also possible to note that the Al/Fe – section J display a different morphology compared to Al/Cu sections. The waves are more elongated than those from Al/Cu.

Two types of defects could be presented on the surfaces, as highlighted in Fig. 4. The pink rectangle (solid lines) in Fig. 4(a) indicate discontinuous local variations in surface height resulting from the surface extraction process as explained in Fig. 5. The issue is coming from the detection step in the program due to insufficient contrast between the feature and its surrounding environment. In the Fig. 5(b), it is possible to see an example of discontinuity on the left side between the tomographic sections 499–500–501. This is due to the segmentation level that is just on the limit for the detection of a new feature. These are linked to the interface detection program which can be discontinuous from frame to frame. Frames 499 and 500 exhibit the initiation of a vortex, which is no longer detected in frames 501 and 502. The blue rectangle (dashed lines)represent horizontal defects caused by tomographic artifacts such as rings or beam hardening during the reconstruction. However, these defects only locally affect the surface and were limited in nature due to a pre-processing of the data during the reconstruction step (see: Materials and methods). The back ellipse (dashed

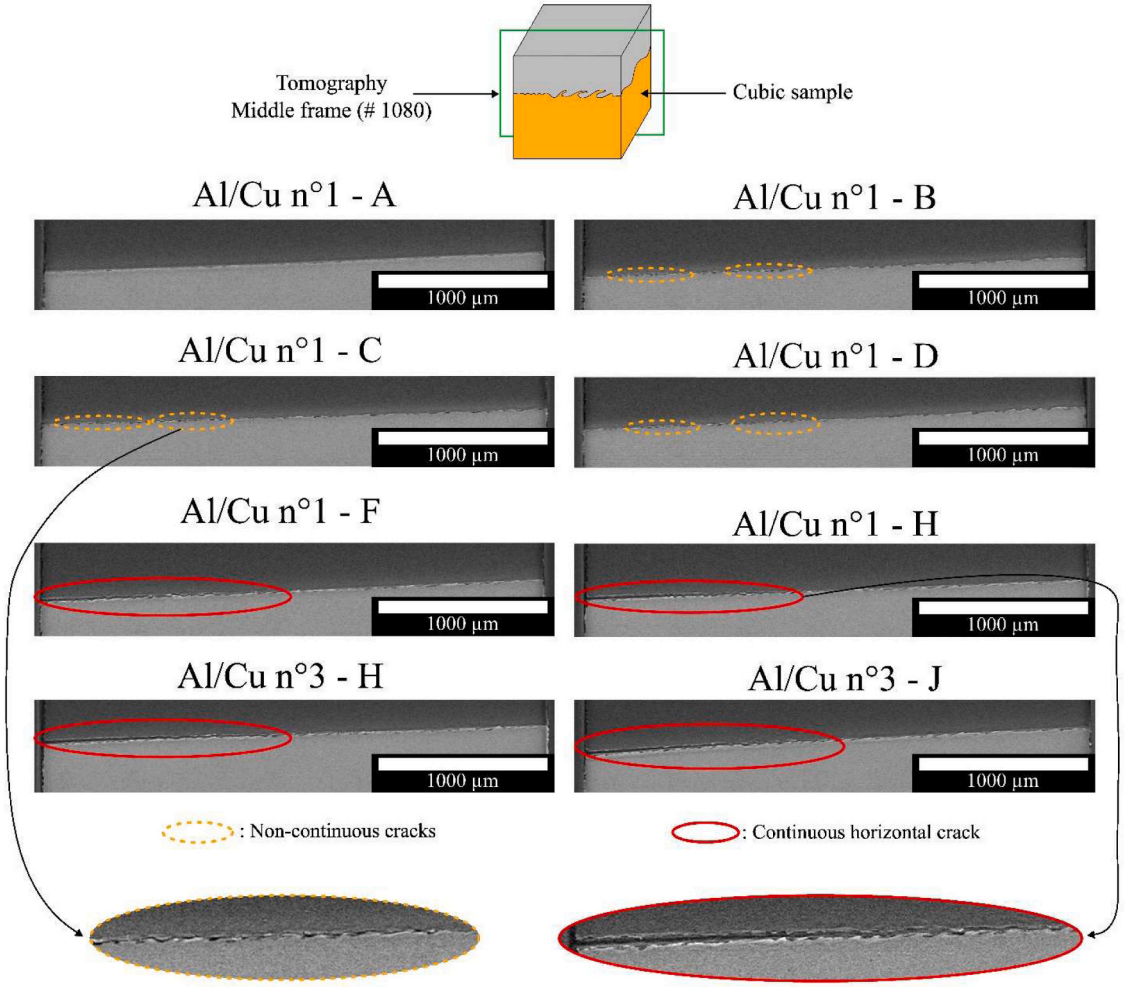

Fig. 10. Cracks comparison at the center of the cubes (frames #1080) – Plan (XZ).

lines) highlights an example of interface reconstructed waves.

The surfaces obtained were considered to have good reconstruction quality after a visual inspecting the segmentation and interface line extraction, as demonstrated in Fig. 5(a). Once the quality was assessed, it became possible to measure topographic roughness parameters and perform quantitative analyses on them.

3.2. Topographic roughness analysis

Before calculating the roughness parameters, a pre-processing step was carried out on all extracted surfaces. First, a third-degree polynomial was used to eliminate the global shape of the surfaces. Second, an S-filter with a 8 µm wavelength was applied to suppress micro-rugosity and high-frequency noise. Finally, roughness parameters were computed on the surfaces following ISO 25178 [40].

The results of the roughness parameters are displayed in Fig. 6. These parameters were calculated for five different metrics (Sa, Sq, Ssk, Sku and Sdr). Sa and Sq represent the arithmetical mean height. ($Sa = \frac{1}{A}\iint_A |Z(x,y)|\,dxdy$) and the mean square height ($Sq = \sqrt{\frac{1}{A}\iint_A Z^2(x,y)dxdy}$) respectively. Sq is equivalent to the standard deviation of heights, while Sa is used to evaluate surface roughness. Ssk (skewness) represents the degree of bias of the roughness shape ($Ssk = \frac{1}{Sq^3}\left[\frac{1}{A}\iint_A Z^3(x,y)dxdy\right]$). A negative Ssk indicates that the surface is skewed above the mean plane, while a positive Ssk indicates that the surface is skewed below the mean plane. Sku (kurtosis) measures the sharpness of the roughness profile ($Sku = \frac{1}{Sq^4}\left[\frac{1}{A}\iint_A Z^4(x,y)dxdy\right]$). When Sku > 3, the height distribution is spiked whereas with Sku < 3, the height distribution is skewed below the mean plane. Sdr is the surface interfacial developed ratio compared to a planar definition area

$$(Sdr = \frac{1}{A}\left[\iint_A \left(\sqrt{\left[1+\left(\frac{\partial Z(x,y)}{\partial x}\right)^2+\left(\frac{\partial Z(x,y)}{\partial y}\right)^2\right]}-1\right)dxdy\right].$$

The results show that the roughness parameters vary along the lateral position of the section. For Al/Cu sample 2, there was an increase in the roughness parameters (Sa, Sq, Sdr) for sections A, B, C and D, followed by a plateau for sections F and H. This stabilization and plateau were also observed for samples number 1 and 3, specifically in their sections (H, J, and K). These results suggest that roughness parameters from sections in similar locations are equivalent, indicating that the surfaces are also similar. This confirms that the MPW process is repeatable between the welding joints and it produces joints that have similar properties in the same location (H for example) across different welds (n°1 and 2). Ssk and Sku for section H3 are slightly affected due to a notable cavity detected by the micro-tomography.

The roughness parameters of Al/Fe sample differed from the others. As explained previously in the Section 3, this particular sample is a joint of Al/Fe, while the others are Al/Cu assemblies. The differences in the Ssk and Sku parameters indicated that the surface morphology of Al/Fe sample was distinct from Al/Cu samples 1, 2 and 3. The Sa, Sq and Sdr

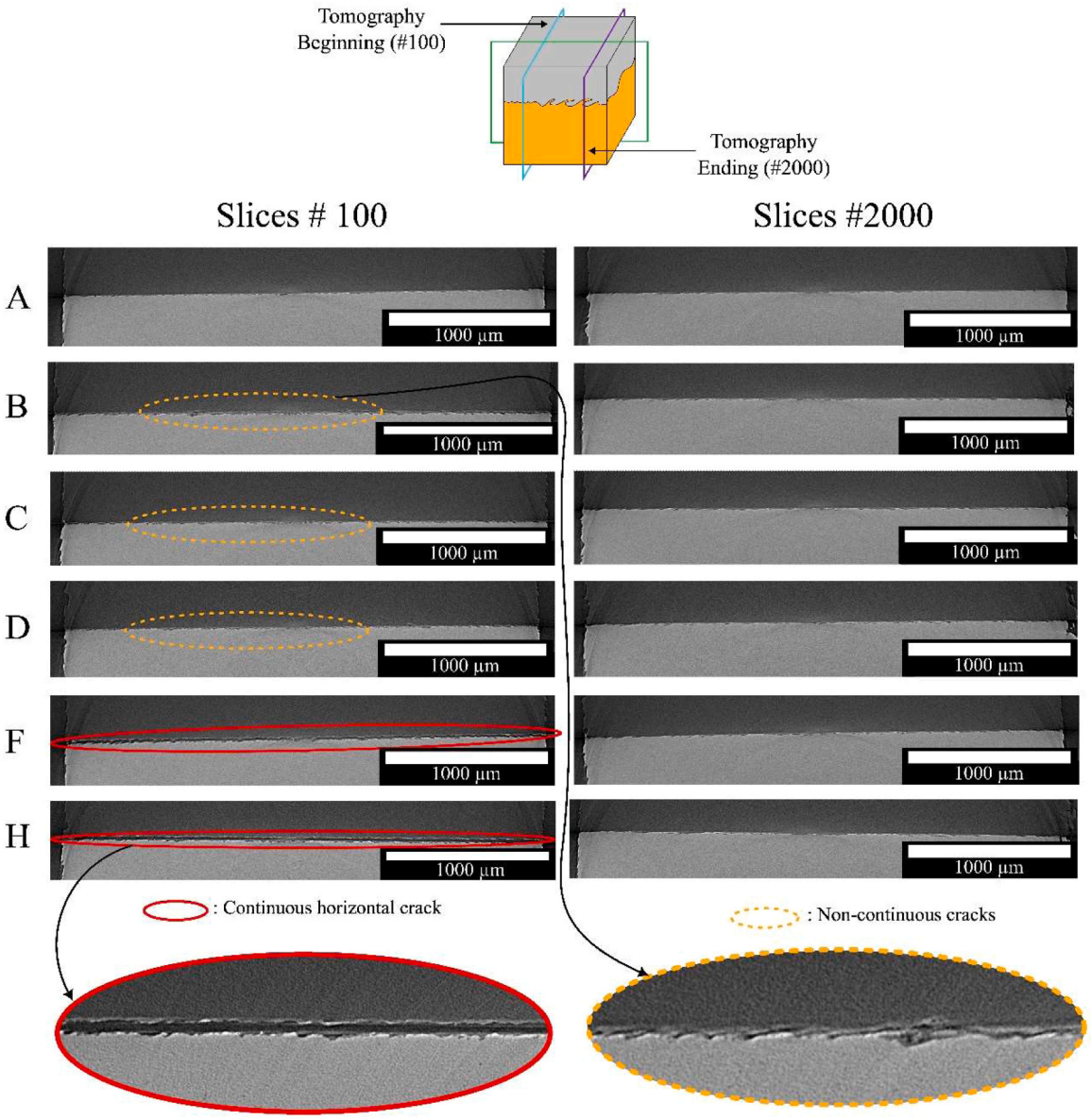

Fig. 11. Cracks comparison at the beginning and ending of the cubes (frames #100 and #2000) – Plan (YZ).

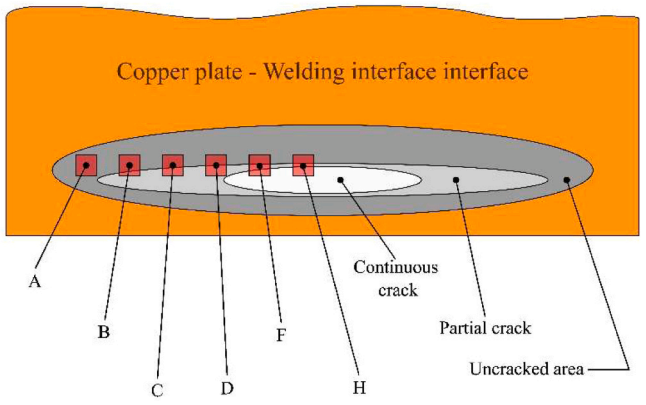

Fig. 12. Location of the cubic samples from the weld and a prediction of the welding interface.

parameters of Al/Fe sample (section J) were equivalent to the roughness and developed surface of section A in the case of an Al/Cu assembly.

While the topographic roughness parameters provide information about the type of surfaces interface and enable quantitative comparisons, they are unable to precisely describe the morphology of the different interface features. Therefore, it is important to visually observe and describe these distinct features.

3.3. *Interface feature morphology*

The interface of MPW joints is known to exhibit distinct features [22], including flatness, waviness, cavities or vortexes. These features are not initiated by the magnetic field but rather by the mechanical conditions (stress, strain, temperature) at the interface as indicated by Hunt [41] for similar features in explosive welding. Waves and vortexes are orientated according to the welding direction (collision point). Previous studies have numerically predicted the formation of such features, but only in a cross-section [39]. By utilizing synchrotron high-energy phase-contrast micro-tomography, 3D information about the morphological structure (ex-situ) of waves along the lateral direction

can be obtained with unprecedented detail.

Fig. 7 illustrates an example of the information that can be obtained, along with a comparison to standard optical imaging methods such as optical microscopy. Frames #7 to #22 showcase the observable growth and shrinkage of a cavity along the slicing direction (indicated by a red circle with a solid line) at the interface for one sample.

Porosities and cavities from Fig. 7 have been extracted and rendered in DragonFly and Fig. 8 displays them. Porosities are not interconnected between themselves and are isolated confirming the results obtained into the cross-sections. However, X-ray allowed to evaluate their shapes into 3D. Thus, it is possible to specify that they do not present spherical shapes but more ellipsoid shapes instead. These porosities and cavities have been predicted by numerical simulations as shown by Li et al. [23]. Simulations were conducted in 2D sections, but they anticipate spherical shapes for micro and meso-scale porosities. These porosities are formed during the ultra-high heating, combined with rapid expansion due to depressurization and rapid cooling. This initiates a sequence of pore nucleation, coalescence, and growth within the molten layer. The intense swirling that forms the vortexes creates favorable conditions for preserving this empty space.

interfacial features were classified based on their morphologies. The term “wave” refers to a shape without swirling and can be considered as a “hill”. On the other hand, the term “vortex” indicates a shape with a swirling motion at its end.

The formation of vortexes was observed, as shown in the example depicted in Fig. 7 with the yellow square (dashed lines) spanning frames #1 to #40. In frames #4 and #25, the crest of the vortex was not continuous and appeared broken into two pieces. However, other vortexes remained continuous, as highlighted within the green ellipse (dashed lines). This vortex maintained its overall shape without any broken parts. However, there was an evolution at the center of the vortex, transitioning from a cavity to some intermetallic compounds (IMC). Some of the IMCs were also visible on the optical image in Fig. 7 (b). Blue squares (solid lines) indicated vortexes or broken parts, which were evident between frames #7 and #16 on the right side, where a portion of the vortex was segmented and distributed across different frames. The information obtained through synchrotron micro-tomography (Fig. 7(a)) complemented the standard optical inspection (Fig. 7(b)) by enabling the study of vortex evolution and understanding the origin of some copper fragments found inside the IMC pockets in the optical images. Indeed, these copper fragments originated from broken portions of vortexes.

It should also be noted that the Al/Cu section displayed in Fig. 7(b) is not exactly the same as the frames shown in the tomographic images. Obtaining a cross-section cut with the exact same orientation and position as the tomographic scans is very complex. Therefore, the decision was made to cut another equivalent sample section. Overall, phase-contrast micro-tomography may not achieve to the same level of clarity as standard optical 2D cross-sections, but it does enable the examination of the 3D evolution of waves and vortexes that is inaccessible through optical images.

In this section, the morphology of waves and vortexes was described. It was observed that waves and vortexes evolve laterally, with the growth and collapse of these features. Vortexes were categorized into two types; standard vortexes and broken vortexes. Broken vortexes can explain the origin of copper fragments that become detached from the base plate at the interface during impact.

3.4. Vortex parameters

Vortexes features at the interface play a significant role in interfacial quality since they represent the interlocking of materials in the joint. Several key parameters describing this vortex morphology were evaluated from the various types of surfaces. These parameters include; the mean number of detected vortexes per frame, mean surface area per vortex (in μm^2), and the mean difference in vortex location along the x-axis (parallel to the welding direction) for each surface. The vortex area is calculated as a right triangular surface. The base line corresponds to the distance between the begin and the end of the vortex (x-axis), whereas the height is the amplitude of the vortex (z-axis). The distance between the vortexes is calculated from theirs beginning. The methodology to detecting the beginning of the vortexes is described in a previous article (see [37]).

The extracted results are depicted in Fig. 9. The mean vortex surface (Fig. 9(b)) provides complementary information to the topographic roughness parameters. The Al/Fe sample (J) exhibited the lowest average value for vortex surface area. In the case of Al/Cu samples, there was a relatively good stability among identical sections from different samples. However, it should be noted that vortex areas in sections H and J in samples 2 and 3 were slightly broader than those in sample 1. In sample 1, the vortex areas showed an increase before reaching stabilization or maximum.

Fig. 9(a) and (c) depict the average number of detected vortexes per frame (per tomographic slice) and the distance between them. Sample Al/Fe (J) had the lowest number of vortexes per frame with the wider distance between them. This, along with the small area for each vortex, explains the limited values for the topographic roughness parameters (Sa, Sq, and Sdr).

It is worth noting that the distance between the vortexes in samples 1 and 2 across different sections remained stable. Section A of sample 1 exhibited a similar behavior to Al/Fe sample n°J, with a small vortex surface and a limited number of vortexes per frame. In contrast, sample Al/Cu n°1 – B demonstrated a different behavior, with a below-average surface area per vortex but a higher number of vortexes per frame. These two parameters account for the higher value of the Sdr parameter shown in Fig. 6(e). Thus, it is possible to conclude that a higher number of vortexes with smaller surface areas can lead to the formation of a more significant contact area between dissimilar materials compared to a few vortexes with larger surface areas. Other sections of sample 1 exhibited a decrease in the number of vortexes per frame until reaching a plateau.

These results serve to illustrate the contrasting interfaces achieved between Al/Cu and Al/Fe samples through MPW. Despite employing the same process parameters (energy, gap) and impact conditions (velocity and angle), the resulting interfaces and their characteristics are notably distinct. This distinction can be attributed to the differing mechanical properties of copper and steel, with copper being more ductile and prone to deformation than steel.

The analysis of the vortex parameters allowed the identification and explanation of variations observed in the topographic roughness parameters mentioned in Section 3.2. Additionally, it highlighted the specificity of section B in sample 1, which acted as the pivotal point in transitioning from the initial behavior observed in section A to a stabilized interface. It is important to note that these results are calculated based on the entire extracted surface at the interface.

3.5. Interfacial fractures

Besides the vortexes observed at the interface, interfacial fractures were also detected in the different samples. These cracks were found not to be randomly positioned but to be at the sides of the samples. Fig. 10 shows the interface extracted from the middle of the tomographic frame of welds n°1 and n°3 within the (XZ) plan.

The first sample (Al/Cu n°1-A) showed no sign of cracks. This sample interface was considered as a sound weld. On the other hand, Al/Cu n°1 B, C, and D exhibited partial and discontinuous cracks at the interface between copper and aluminum (as seen in Fig. 10).

On the other hand, the samples Al/Cu n°1 F, H, and Al/Cu n°33 H, and J displayed more damage at the interface. The discontinuous cracks evolved into a continuous horizontal crack spanning the entire sample (as shown in Fig. 10). Fig. 11 displays the discontinuous and continuous cracks of the samples within the (YZ) plan. This view complements the previous one from Fig. 10 and shows that the continuous cracks run through the entire sample along the y-axis (refer to slices #100).

Additionally, it illustrates the evolution of the morphological structure of the interface across the different sections.

Fig. 12 describes the positions of the extracted cubic samples within the weld and also Fig. 12 illustrates the different types of interfaces observed on the sample interfaces.

The presence of a continuous crack can have a substantial impact on the mechanical behavior of the entire assembly, as demonstrated in the authors' previous study [42]. These continuous horizontal cracks are considered to be equivalent to a completely unwelded zone, as described by Geng et al. [43]. The authors suggested that no welding occurred at the center of the joint due to an insufficient impact angle which would not stimulate the formation of a jet and hence material mixing and joining.

However, it was observed that welding initially took place along the continuous cracked interface, but subsequently got separated. This is evident from the presence of complementary shapes on both sides of the cracked interface. These complementary shapes consist of copper or intermetallic compounds. This finding is consistent with studies that have shown and the presence of a melted layer that can crack at the interface [44]. Thus, the unwelded zone corresponds to an area where welding occurred (with interlocking of the interface) and then got separated before the end of the welding process.

Furthermore, with the support of synchrotron tomography, it is possible to describe the unwelded zone as composed of two different areas; one with a continuous interfacial fracture (at the center of the welding seam – sections F to J) and another area with partial cracking surrounding the previous one (sections B to D from the welding seam) as shown in Fig. 12.

4. Conclusions

In this study, the morphology of the interface between dissimilar materials (Al/Cu and Al/Fe) welded by MPW was examined in three dimensions (3D).

First, a specific method was developed to extract the joint interface surface using synchrotron tomography. These surfaces were quantified and compared by applying topographic roughness parameters. Additionally, a classification of the interface features was proposed and evaluated. Finally, a study was conducted on the occurrence and positions of cracks.

The main findings of this study can be summarized as follows:

1) Surface roughness parameters (Sa, Sq, and Sdr) of the joint interface varied laterally, transitioning from a relatively flat surface at the edges to a rougher surface at the center of the weld before reaching a plateau.
2) Surface roughness parameters showed similarities among different sections of the weld located at the same position, confirming the repeatability of the MPW process.
3) Vortexes and waves exhibited longitudinal (in the welding direction) as well as lateral evolution, resulting in a complex 3D interlocking surface between the welded materials due to the vortexes swirling, the presence of intermetallic compounds (IMCs) and fragmented vortex pieces.
4) The interface morphology of Al/Cu and Al/Fe samples differed under similar welding process and impact condition. The Al/Fe interface displayed fewer vortexes and lower roughness compared to the Al/Cu samples, highlighting the influence of material properties on interface morphology for welding performed under the same process parameters.
5) The presence of annular welds could indicate a poor-quality weld due to the continuous crack located at the center of the weld. This crack shows signs that welding occurred, but then the interface got separated and could result from an inadequate selection of welding process parameters.

Funding

This research did not receive any specific grant from funding agencies in the public, commercial or nonprofit sectors.

CRediT authorship contribution statement

Benjamin Zielinski: Conceptualization, Methodology, Software, Investigation, Writing – original draft, Visualization. **Tarik Sadat:** Conceptualization, Methodology, Validation, Investigation, Writing – review & editing. **Bratislav Lukić:** Validation, Investigation, Writing – review & editing **Alexander Rack:** Resources, Writing – review & editing, Project administration. **Eric Markiewicz:** Resources, Writing – review & editing, Supervision, Project administration, Funding acquisition **Laurent Dubar:** Resources, Writing – review & editing, Supervision, Project administration, Funding acquisition.

Declaration of Competing Interest

The authors declare that they have no known competing financial interests or personal relationships that could have appeared to influence the work reported in this paper.

Acknowledgements

The authors would like to thank the MorphoMeca platform for the use of the measuring apparatus and software. The authors would also like to thank the PFT Innovaltech and M. Denis Jouaffre for the supply of the MPW joints. ESRF is thanked for beamtime at ID19.

References

[1] J.D. Achenbach, Quantitative nondestructive evaluation, Int. J. Solids Struct. 37 (2000) 13–27, https://doi.org/10.1016/S0020-7683(99)00074-8.
[2] A. Sophian, G. Tian, M. Fan, Pulsed eddy current non-destructive testing and evaluation: a review, Chin. J. Mech. Eng. (Engl. Ed. 30 (2017) 500–514, https://doi.org/10.1007/s10033-017-0122-4.
[3] S.K. Dwivedi, M. Vishwakarma, P.A. Soni, Advances and researches on non destructive testing: a review, Mater. Today Proc. 5 (2018) 3690–3698, https://doi.org/10.1016/j.matpr.2017.11.620.
[4] J. Banhart, éd., Advanced Tomographic Methods in Materials Research and Engineering, (2008). https://doi.org/10.1093/acprof:oso/9780199213245.001.0001.
[5] A.T. Polonsky, J.D. Madison, M. Arnhart, H. Jin, K.N. Karlson, A.J. Skulborstad, J. W. Foulk, S.G. Murawski, Toward accurate prediction of partial-penetration laser weld performance informed by three-dimensional characterization – part I: high fidelity interrogation, Tomogr. Mater. Struct. 2 (2023), 100006, https://doi.org/10.1016/j.tmater.2023.100006.
[6] E. Maire, P.J. Withers, Quantitative X-ray tomography, Int. Mater. Rev. 59 (2014) 1–43, https://doi.org/10.1179/1743280413Y.0000000023.
[7] R. Khajeh, H.R. Jafarian, S.H. Seyedein, R. Jabraeili, A.R. Eivani, N. Park, Y. Kim, A. Heidarzadeh, Microstructure, mechanical and electrical properties of dissimilar friction stir welded 2024 aluminum alloy and copper joints, J. Mater. Res. Technol. 14 (2021) 1945–1957, https://doi.org/10.1016/j.jmrt.2021.07.058.
[8] R.P. Mahto, R. Kumar, S.K. Pal, Characterizations of weld defects, intermetallic compounds and mechanical properties of friction stir lap welded dissimilar alloys, Mater. Charact. 160 (2020), 110115, https://doi.org/10.1016/j.matchar.2019.110115.
[9] M. Sokac, I. Budak, M. Katic, Z. Jakovljevic, Z. Santosi, D. Vukelic, Improved surface extraction of multi-material components for single-source industrial X-ray computed tomography, Meas. J. Int. Meas. Confed. 153 (2020), 107438, https://doi.org/10.1016/j.measurement.2019.107438.
[10] A. Townsend, R. Racasan, R. Leach, N. Senin, A. Thompson, A. Ramsey, D. Bate, P. Woolliams, S. Brown, L. Blunt, An interlaboratory comparison of X-ray computed tomography measurement for texture and dimensional characterisation of additively manufactured parts, Addit. Manuf. 23 (2018) 422–432, https://doi.org/10.1016/j.addma.2018.08.013.
[11] A.R. Zekavat, A. Jansson, C. Gundlach, L. Pejryd, Effect of X-ray Computed Tomography Magnification on Surface Morphology Investigation of Additive Manufacturing Surfaces, ICT Conf. 2018, Wels, Austria, 7 February, 2018. (2018). ⟨http://hj.diva-portal.org/smash/get/diva2:1548607/FULLTEXT01.pdf⟩.
[12] F. Zanini, E. Sbettega, M. Sorgato, S. Carmignato, New approach for verifying the accuracy of X-ray computed tomography measurements of surface topographies in additively manufactured metal parts, J. Nondestruct. Eval. 38 (2019) 1–10, https://doi.org/10.1007/s10921-018-0547-4.

[13] A.M. Venkatesh, D. Bouvard, P. Lhuissier, J. Villanova, 3D analysis of ceramic powder sintering by synchrotron X-ray nano-tomography, J. Eur. Ceram. Soc. 43 (2023) 2553–2563, https://doi.org/10.1016/j.jeurceramsoc.2022.12.065.
[14] M. Cotte, P.O. Autran, C. Berruyer, C. Dejoie, J. Susini, P. Tafforeau, Cultural and natural heritage at the ESRF: looking back and to the future, Synchrotron Radiat. News 32 (2019) 34–40, https://doi.org/10.1080/08940886.2019.1680213.
[15] R.M. Miranda, B. Tomás, T.G. Santos, N. Fernandes, Magnetic pulse welding on the cutting edge of industrial applications, Soldag. Insp. 19 (2014).
[16] H. Wang, Y. Wang, High-velocity impact welding process: A review, Metals 9 (2019), https://doi.org/10.3390/met9020144.
[17] S. Kudiyarasan, S. Arungalai Vendan, Magnetic pulse welding of two dissimilar materials with various combinations adopted in nuclear applications, Indian J. Sci. Technol. 8 (2015), https://doi.org/10.17485/ijst/2015/v8i36/88513.
[18] A. Jöckel, A. Maciolek, J. Baumgartner, B. Möller, S. Völkers, M. Graß, S. Böhm, Fatigue strength assessment of laser beam welded joints made of AA7075 and magnetic pulse welded joints made of AA7075 and 3D-printed AlSi10Mg, Adv. Eng. Mater. (2023), 2300108, https://doi.org/10.1002/adem.202300108.
[19] Y. Zhou, C. Li, X. Shi, P. Wang, T. Shen, Y. Mi, Y. Ma, Evaluation model of electromagnetic pulse welding effect based on Vc-β trajectory curve, J. Mater. Res. Technol. 20 (2022) 616–626, https://doi.org/10.1016/j.jmrt.2022.07.069.
[20] A. Kapil, A. Sharma, Magnetic pulse welding: an efficient and environmentally friendly multi-material joining technique, J. Clean. Prod. 100 (2015) 35–58, https://doi.org/10.1016/j.jclepro.2015.03.042.
[21] M. Pourabbas, A. Abdollah-Zadeh, M. Sarvari, F. Movassagh-Alanagh, M. Pouranvari, Role of collision angle during dissimilar Al/Cu magnetic pulse welding, Sci. Technol. Weld. Join. 25 (2020) 549–555, https://doi.org/10.1080/13621718.2020.1768351.
[22] A. Ben-Artzy, A. Stern, N. Frage, V. Shribman, O. Sadot, Wave formation mechanism in magnetic pulse welding, Int. J. Impact Eng. 37 (2010) 397–404, https://doi.org/10.1016/j.ijimpeng.2009.07.008.
[23] J.S. Li, R.N. Raoelison, T. Sapanathan, Y.L. Hou, M. Rachik, Interface evolution during magnetic pulse welding under extremely high strain rate collision: mechanisms, thermomechanical kinetics and consequences, Acta Mater. 195 (2020) 404–415, https://doi.org/10.1016/j.actamat.2020.05.028.
[24] T.Z. Blazynski, Explosive Welding, Forming and Compaction, Springer,, Netherlands, Dordrecht, 1983, https://doi.org/10.1007/978-94-011-9751-9.
[25] W. Zhang, Y. Chen, J. Xie, T. Zhang, S. Wang, X. Song, L. Yin, Interfacial microstructure of Al/Ta dissimilar joints by magnetic pulse welding, J. Mater. Res. Technol. 23 (2023) 4167–4172, https://doi.org/10.1016/j.jmrt.2023.02.065.
[26] T. Lee, S. Zhang, A. Vivek, G. Daehn, B. Kinsey, Wave formation in impact welding: study of the Cu–Ti system, CIRP Ann. 68 (2019) 261–264, https://doi.org/10.1016/j.cirp.2019.04.058.
[27] J. Li, R.N. Raoelison, T. Sapanathan, M. Rachik, Determining the weldability window based on the interface morphologies formed during high-speed collision in magnetic pulse welding, Sci. Technol. Weld. Join. (2022) 1–9, https://doi.org/10.1080/13621718.2022.2151733.
[28] R.N. Raoelison, N. Buiron, M. Rachik, D. Haye, G. Franz, Efficient welding conditions in magnetic pulse welding process, J. Manuf. Process. 14 (2012) 372–377, https://doi.org/10.1016/j.jmapro.2012.04.001.
[29] R.N. Raoelison, N. Buiron, M. Rachik, D. Haye, G. Franz, M. Habak, Study of the elaboration of a practical weldability window in magnetic pulse welding, J. Mater. Process. Technol. 213 (2013) 1348–1354, https://doi.org/10.1016/j.jmatprotec.2013.03.004.
[30] T. Weitkamp, P. Tafforeau, E. Boller, P. Cloetens, J. Valade, P. Bernard, F. Peyrin, W. Ludwig, L. Helfen, J. Baruchel, Status and evolution of the ESRF beamline ID19, AIP Conf. Proc. 1221 (2010) 33–38. https://doi.org/10.1063/1.3399253.
[31] H. Payno, P. Paleo, C. Nemoz, P. Cloetens, M. Di Michiel, A. Rack, P. Tafforeau, V. A. Solé, N.R. Viganò, Overcoming the data processing challenges of unifying tomography techniques at ESRF, J. Phys. Conf. Ser. 2380 (2022) 6–11, https://doi.org/10.1088/1742-6596/2380/1/012106.
[32] D. Paganin, S.C. Mayo, T.E. Gureyev, P.R. Miller, S.W. Wilkins, Simultaneous phase and amplitude extraction from a single defocused image of a homogeneous object, J. Microsc. 206 (2002) 33–40, https://doi.org/10.1046/j.1365-2818.2002.01010.x.
[33] C. Raven, Numerical removal of ring artifacts in microtomography, Rev. Sci. Instrum. 69 (1998) 2978–2980, https://doi.org/10.1063/1.1149043.
[34] Object Research Systems (ORS), Dragonfly sofwtare, (s. d.). ⟨http://www.theobjects.com/dragonfly⟩.
[35] MATLAB - 2023a, (2023). https://fr.mathworks.com/products/matlab.html.
[36] Digital Surf, Digital Surf - Mountains software, (2022). https://www.digitalsurf.com/ (consulté le 29 septembre 2022).
[37] B. Zielinski, T. Sadat, R. Guibert, D. Jouaffre, E. Markiewicz, L. Dubar, Interface morphology description and quantification of Al – Cu magnetic pulse welding joints using X-Ray micro-computed tomography, J. Nondestruct. Eval. 123 (2023), https://doi.org/10.1007/s10921-023-00984-4.
[38] Z. Xu, J. Cui, H. Yu, C. Li, Research on the impact velocity of magnetic impulse welding of pipe fitting, Mater. Des. 49 (2013) 736–745, https://doi.org/10.1016/j.matdes.2012.12.059.
[39] J.S. Li, T. Sapanathan, R.N. Raoelison, Y.L. Hou, A. Simar, M. Rachik, On the complete interface development of Al / Cu magnetic pulse welding via experimental characterizations and multiphysics numerical simulations, J. Mater. Process. Technol. 296 (2021), https://doi.org/10.1016/j.jmatprotec.2021.117185.
[40] International Organization for Standardization, ISO 25178–2:2021 - Geometrical product specifications (GPS) — Surface texture: Areal — Part 2: Terms, definitions and surface texture parameters, 2021. ⟨https://www.iso.org/standard/74591.html⟩.
[41] J.N. Hunt, Wave formation in explosive welding, Philos. Mag. 17 (1968) 669–680, https://doi.org/10.1080/14786436808223020.
[42] B. Zielinski, T. Sadat, B. Lukić, G. Haugou, H. Morvan, A. Rack, E. Markiewicz, L. Dubar, Characterization of local mechanical properties of Al/Cu magnetic pulse welded joints under high strain rates using synchrotron X-ray imaging, Mater. Lett. 337 (2023), https://doi.org/10.1016/j.matlet.2023.133943.
[43] H. Geng, Z. Xia, X. Zhang, G. Li, J. Cui, Microstructures and mechanical properties of the welded AA5182/HC340LA joint by magnetic pulse welding, Mater. Charact. 138 (2018) 229–237, https://doi.org/10.1016/j.matchar.2018.02.018.
[44] A. Nassiri, G. Chini, A. Vivek, G. Daehn, B. Kinsey, Arbitrary Lagrangian-Eulerian finite element simulation and experimental investigation of wavy interfacial morphology during high velocity impact welding, Mater. Des. 88 (2015) 345–358, https://doi.org/10.1016/j.matdes.2015.09.005.